

ERNST-MORITZ-ARNDT UNIVERSITY OF
GREIFSWALD

MASTER THESIS

Kinetic effects in RF discharges

Author:
Philipp Hacker

Supervisor:
Prof. Dr. Ralf Schneider

*A thesis submitted in fulfillment of the requirements
for the degree of Master of Science - Physics*

in the research group of

Computational Sciences,
Institute of Physics



August 28, 2017

Declaration of Authorship

I hereby certify that this thesis has been composed by me and is based on my own work, unless stated otherwise. No other person's work has been used without due acknowledgement in this thesis. All references and verbatim extracts have been quoted, and all sources of information, including graphs and data sets, have been specifically acknowledged.

.....

Signature of author
Greifswald; August 28, 2017

Contents

Motivation	1
1 Physical Properties of Low Temperature RF Plasma	3
1.1 Plasma Physics	3
1.1.1 Capacitively Coupled Radio Frequency Plasma	3
1.1.2 Plasma-Wall Interaction	4
1.1.2.1 Child-Langmuir Law	4
1.1.3 Bohm Criteria	5
1.1.3.1 Surface Effects	7
1.1.4 Self Bias Voltage	9
1.1.5 Dielectric Displacement Current	10
1.1.6 Heating Mechanisms	11
1.2 Oxygen Plasma Chemistry	14
1.2.1 Collisions and Reactions	15
1.2.2 Anion Species	16
1.3 Particle-in-Cell Simulations with Monte Carlo-Colissions	17
1.3.1 Principles	18
1.3.2 2d3v PIC	20
1.3.3 Monte Carlo-Collisions	23
2 Validation of Simulation by 1d comparison	25
2.1 Axial density profiles	25
2.2 Velocity and energy distributions	25
2.3 Transition to 2d simulation	25
3 Simulation of capacitively coupled rf discharges	27
3.1 Experimental setup	27
3.1.1 Reference Discharge	27
3.1.2 Simulated Discharge	28
3.2 Simulated ccrf Oxygen Discharge	30
3.3 Anion Energy Distributions in Oxygen	30
4 Conclusion	31
A Appendix	33
Bibliography	35

List of Abbreviations

abbreviation	full expression
e.g.	exempli gratia; <i>for example</i>
etc.	et cetera; <i>and so on</i>
ac	alternating current
dc	direct current
rf, RF	radio frequency
ccrf	capacitively coupled radio frequency
EDF	energy distribution function
EDV	<i>german: Energieverteilungsfunktion</i> , energy distribution function
EEDF	electron energy distribution function
IEDF	ion energy distribution function
p., pp.	page, plural pages
ff.	folio; <i>on the (next) page</i> , ablative of folium (<i>page</i>)
SIE, SEE	secondary ion/electron emission
HWA	hard wall approximation
MS	mass spectrometer
PROES	phase resolved emission spectroscopy
MWI	microwave interferometer
AN	antenna
FC	flow controller
PIC	particle-in-cell
MCC	Monte-Carlo-Colissions

abbreviation	full expression
--------------	-----------------

Table 1: List of abbreviations and their corresponding phrases. If specified, the translation or an equivalent expression is written.

Physical Quantities

Quantity	Unit	Symbol	Dimension	Value
Speed of Light	m/s	c_0	L^1T^{-1}	$2.997 \cdot 10^8$
thermal velocity	m/s	$v_{th,j}$	L^1T^{-1}	
drift velocity	m/s	$v_{D,j}, u_j$	L^1T^{-1}	
Boltzmann constant	eV/K	k_B	$M^1L^2T^{-2}K^{-1}$	$8.617 \cdot 10^{-23}$
mobility	cm^2/Vs	μ_j	$I^1T^2M^{-1}$	
planck constant	eVs	\hbar	$G^{-1/2}c^{6/2}\epsilon_0^{1/2}$	$4.1345 \cdot 10^{-15} \text{ eVs}$ $6.646 \cdot 10^{-34} \text{ Js}$
kinetic temperature	eV	T_j	$M^1L^2T^{-2}$	$1 \text{ eV} = 1.902 \cdot 10^{-19} \text{ K}$
elementary charge	C	e	I^1T^1	$1.902 \cdot 10^{-19}$
electric charge	C	Q, q	I^1T^1	
particle mass	kg	m_j	M^1	electron: $9.109 \cdot 10^{-31}$ ion: $5.310 \cdot 10^{-26}$ anion: $5.143 \cdot 10^{-26}$
reduced mass	kg	$\mu_{j,k}$	M^1	
distance,location	cm	r, \vec{r}	L^1	
Debye length	cm	$\lambda_{D,j}$	L^1	
particle distance	cm	\bar{b}	L^1	
mean free path	cm	$s_{mfp,j}$	L^1	
particle density	cm^{-3}	n_j	L^{-3}	
Vacuum permittivity	F/m	ϵ_0	$M^{-1}L^{-3}T^{-4}A^2$	$8.854 \cdot 10^{-12}$
electrostatic potential	V	Φ, U	$M^1L^2I^{-1}T^{-3}$	
electric current	As	I, J	I^1	
electric current density	As/cm^2	j_j	I^1L^{-2}	
electric charge density	C/cm^3	ρ	$I^1T^1L^{-3}$	

Quantity	Unit	Symbol	Dimension	Value
electric resistance	Ω	R	$M^1 L^2 T^{-3} I^{-2}$	
electric capacity	F	C	$M^{-1} L^{-2} T^4 I^2$	
time	s	t	T^1	
plasma frequency	Hz	$\omega_{p,j}$	T^{-1}	
collisional frequency	Hz	ν_j	T^{-1}	

Table 2: Physical properties in their commonly — or for this purpose most convinient — units and corresponding SI units. If not specified, the values of each quantity refer to the afore-mentioned units.

Motivation

Chapter 1

Physical Properties of Low Temperature RF Plasma

In this first chapter I will provide the necessary physical background for this work about the numerical simulation of low temperature capacitively coupled radio frequency plasmas. Here, both the simulation method as well as the most important aspects about the plasma properties will be introduced.

1.1 Plasma Physics

1.1.1 Capacitively Coupled Radio Frequency Plasma

The experiment studied in this work is a capacitively coupled radio frequency discharge with a low temperature plasma, operated at low pressures. Here, I will refer to a plasma as a globally quasi-neutral gas, consisting of freely moving charges — e.g. electrons, positively and negatively ions — with additional neutral gas particles. The density ratio between charged and the sum of neutral and charged species defines the *degree of ionization*, which in this case is very low, e.g. below 1%. Charge separation and violation of quasi-neutrality, which means $n_e = n_i$, is only possible for distances below the *Debye length* λ_D .

The creation of a plasma is accomplished by two parallel metal electrodes, where on at least one an ac signal at radio frequency is applied. In the experiment a rf signal at 13.56 MHz with an amplitude between 100–1000 V is used. This results in a wavelength of 22.11 m for the electric field wave, which is orders of magnitude larger than the size of the experiment, which is usually below 10 cm. Many different electric setups are possible, such as coated or grounded electrodes, producing different operational regimes. Such a system resembles a dielectric hindered plate capacitor. This simplification can be used to understand important physical properties, such as an additional voltage offset on one of the electrodes or charge currents. A basic scheme of an asymmetric rf discharge can be seen in figure 1.1. For example, non-biased metal surfaces accumulate a negative potential due to the separation and higher mobility of the electrons. The same goes for electrodes with negative potential and grounded walls. Because continuity has to be satisfied, e.g. electron current onto the wall equals ion current, the spatially restricted area of the *plasma sheath* is established.

Because continuity has to be satisfied, e.g. electron current onto the wall equals ion current, the spatially restricted area of the *plasma sheath* is established. Inside this sheath the electron density drops exponentially towards the wall, where as the ions are accelerated to *Bohm velocity* (see section 1.1.3). In the case of different electrode sizes the potential inside the sheath can change drastically. If the discharge is driven at radio frequency and an additional capacitance is placed between electrode and generator, the fast charge exchange of electrodes and plasma volume during the collapse of the sheath creates a dc voltage offset, because the capacitor can not be discharged quickly enough. This is called *self bias* (see section 1.1.4). A displacement current between plasma sheath and volume accommodates as a result of the different time scales of particle movement (see section 1.1.5). Especially, self-bias and displacement current play a key role in the following investigations, as a capacitive coupling between electrodes and power supply is difficult to model in a numerical kinetic simulation. Radio frequency plasmas are characterized by their unique transport process inside the sheath and heating mechanisms of charged species. A more in-depth discussion can be found in section 1.1.6.

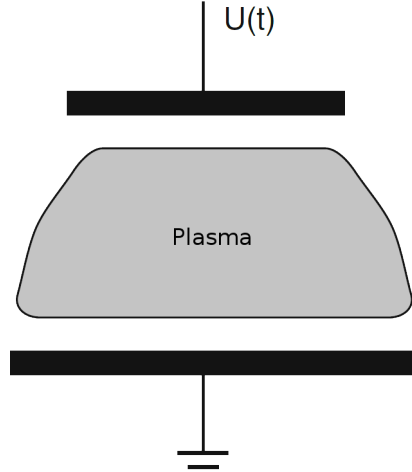


Figure 1.1: Schematic of an asymmetric discharge with one grounded and one driven electrode [12].

1.1.2 Plasma-Wall Interaction

In the bulk of the discharge, neutral gas particles are excited by electron collisions and radiating visible light. However, in rf discharges at low pressures and temperatures the areas around, e.g. floating metal surfaces, probes and grounded walls are darker than the bulk. This is due to the low electron density and kinetic energy in this *plasma sheath*.

Electrons are of a much higher mobility μ_e and thermal velocity $v_{th,e}$. Also they are of a much smaller mass, which is why they are at least $\sqrt{m_i/m_e}$ -times faster than the other species. Hence they impinge onto walls more often, leading to the accumulation of a negative charge and potential around a wall. In the following section the interaction of plasma discharge and walls will be highlighted, emphasizing the difference in dynamics between electron and ion species.

1.1.2.1 Child-Langmuir Law

The *Child-Langmuir Law* yields an expression for the relation between potential and current on a wall in a space-charge limited plasma region, e.g. the sheath. It characterizes transport processes between a floating wall and the plasma bulk. Therefore it is important to understand, for example the oscillation of the sheath boundary in rf plasmas or secondary emission processes at walls.

Let us first assume a negatively charged wall at $x = 0$, which develops a barrier for electrons of thermal velocity, e.g. $|\Phi(0) - \Phi(d)| \ll k_B T_e / e$. The thickness of the sheath here is d and the sheath-boundary therefore at $x = -d$ (see figure 1.2). In an one-dimensional approach [12], the electron density $n_e(x)$ can be written with a *Boltzmann* distribution function $f_B(\Phi) \sim$

$\exp(e\Delta\Phi/k_B T_e)$. This means that the electron density decreases exponentially towards the negatively charged wall. It can be assumed that the sheath thickness $d \ll s_{\text{mfp},i}$ the mean free path of the ions inside the plasma bulk. Hence the ions enter the pre-sheath collisionless at a speed $v_{i,0}$. The ion and electron densities are therefore:

$$n_i(x) = n_i(d) \left(1 - \frac{2e\Phi(x)}{m_i v_{i,0}^2}\right)^{-1/2}, \quad n_e = n_e(d) \exp\left(\frac{e(\Phi(x) - \Phi(d))}{k_B T_e}\right) \quad (1.1)$$

At the boundary between bulk and pre-sheath, the walls potential vanishes because of the plasmas shielding capabilities. Furthermore, one can assume that the kinetic energy of the ions at this point is smaller than the potential energy for the acceleration inside the pre-sheath, e.g. $m_i v_{i,0}^2 \ll |e\Phi(x)|$. Using *Poisson's* equation 1.2 gives an expression for the potential $\Phi(x)$:

$$\Delta\Phi \cong -\frac{en_i(-d)}{\varepsilon_0} \left(-\frac{2e\Phi(x)}{m_i v_{i,0}^2}\right)^{-\frac{1}{2}} \quad (1.2)$$

Solving this, and using the unperturbed ion current $j_i = n_i(d)ev_{i,0}$, one yields the result by *Langmuir* in equation 1.3. Solving this for j_i yields the *Child-Langmuir Law* (see equation 1.4). This equation defines the ion current as a function of the unperturbed plasma bulk. In other words, the sheath changes its thickness in dependency of those certain discharge parameters, always satisfying the ion current defined by the *Child-Langmuir Law*.

$$\Phi(x) = \left(\left(\frac{3}{4}(x+d)\right)^4 \left(\frac{j_i}{\varepsilon_0}\right)^2 \frac{m_i}{2e}\right)^{\frac{1}{3}} \quad (1.3)$$

$$j_i = \frac{4}{9}\varepsilon_0 \left(\frac{2e(\Phi(-d) - \Phi(0))^3}{m_i d^2}\right)^{\frac{1}{2}} \quad (1.4)$$

1.1.3 Bohm Criteria

In section 1.1.2 the behaviour of charged particle densities inside the plasma sheath has been discussed. In contrast to the discharge volume, those densities do not satisfy the quasi-neutrality condition in a distance of d from the wall any more. Because of the negative potential around a wall the transport processes of electrons and ions are perturbed. The potential barrier reflects electrons of low kinetic energies, although both particle species diffuse into the sheath. Their density gradient $\vec{\nabla}n = \vec{\nabla}n_i \approx \vec{\nabla}n_e$ is pointing towards the wall, which can be seen in figure 1.2. Due to their higher mobility electrons have a larger diffusion constant $D_e \gg D_i$ and they are moving much faster to the wall. Because continuity has to be satisfied, e.g. $j_e = j_i$ at the sheath-boundary, negative space charges build up and the corresponding electric fields accelerate the ions to match this condition.

To calculate the exact velocity at which an ion is entering the plasma sheath, the equation of motion has to be solved. Therefore the ion and electron densities from equation 1.1 are substituted into the *Poisson's* equation 1.5.

We know that the acceleration of an ion increases with decreasing distance to the wall because of $\Phi(x)$ in equation 1.2. Therefore the potential derivative of the function $f(\Phi)$ at the sheath-boundary, e.g. $\Phi = 0$, is analogous to the gradient of the electric field in the Maxwell's equation.

$$f(\Phi) = \Delta_r \Phi = \frac{d^2 \Phi}{dr^2} = \frac{\rho}{\epsilon_0} \quad (1.5)$$

$$0 > \left. \frac{df}{d\Phi} \right|_{\Phi=0} = \frac{en_e(-d)}{\epsilon_0} \left(\frac{e}{k_b T_e} - \frac{e}{m_i v_{i,0}^2} \right)$$

$$\Rightarrow v_{i,B} = v_{i,0} \geq \sqrt{\frac{k_B T_e}{m_i}} \quad (1.6)$$

Analogous you can define the so called *Mach number* $M = v_{i,0}/v_{i,B}$, where $v_{i,B}$ denotes the *Bohm velocity*. At the sheath-boundary the quasi-neutrality condition is still satisfied: $n_e = n_i$. The potential $\Phi(x)$ inside the pre-sheath from equation 1.2 and the bulk ion density $n_{i,0}$ from equation 1.1 are now used to describe the ion transport process in the pre-sheath. This is dominated by collisions with neutral gas particles, hence the velocity distribution function has to be rewritten with the ion-neutral collisions frequency $\nu_{n,i}$.

$$\frac{dv_i}{dx} = \frac{\nu_{n,i} v_i^2}{v_B^2 - v_i^2} \quad (1.7)$$

From equation 1.7 we can see: ions with velocities smaller than the Bohm velocity are being accelerated inside the pre sheath. According to equation 1.6 velocities greater than v_B are not allowed. Hence the ion velocity is exactly v_B at the boundary of the plasma sheath.

$$M \geq 1 \Leftrightarrow v_i(-d) \geq v_B \quad (1.8)$$

At $x = -d$, both negative and positive charge density decreased to $n_i = n_e \approx 0.66 n_{e,0}$ (see figure 1.2), where the potential is approximately $-k_B T_e / 2e$ because of the currents onto the wall. In summary, the ion dynamic discussed before is spatially restricted to the sheath and pre-sheath. They only develop where there is electron depletion or an externally applied, negative potential.

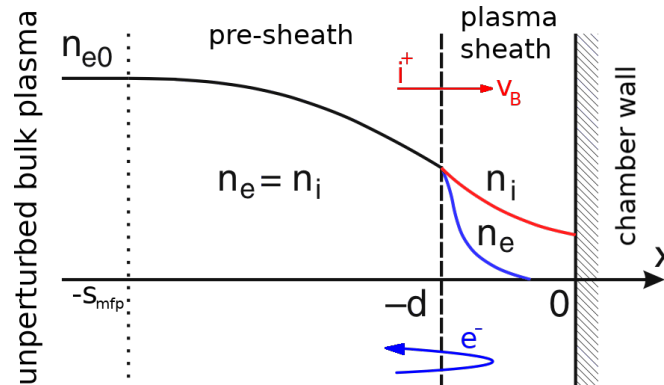


Figure 1.2: One dimensional density profiles as a function of the distance to a floating wall. Note the exponential decrease of the electron density n_e from the sheath border towards the presumably negatively charged wall. Densities already reach approximately $0.66n_{e,0}$ inside the pre-sheath. [12]

1.1.3.1 Surface Effects

Secondary Electron Emission Although the sheath physics is influenced by plasma properties in front of the wall, such as temperatures and densities, it is also sensitive to wall processes. One important aspect is the absorption and re-emission of ions and electrons. Let us first assume that the associated metal wall behind the sheath ideally absorbs all impinging charged particles, which recombine immediately. This is the simplest model, because it only considers recombination. Impinging ions are neutralized by electrons immediately in front of the wall. The resulting ions are reflected and eventually ionized again in the bulk. Because of the large mean free paths of the neutrals and ions, e.g. $s_{\text{mfp}} > d$, this entry and exit process can be considered collisionless.

Like it was highlighted above, the electrons are much faster and more mobile than the other species, leading to a negative charging and potential drop towards the wall. This accelerates the ion species up to *Bohm velocity*. Continuity and charge conservation must be satisfied, hence the charge current densities $j_e = j_i$ must be equal at the sheath edge. The potential drop $\Delta\Phi$ reflects negative charges slower than $v \leq \sqrt{2e\Delta\Phi/m}$. Similar to equation 1.1, the electron current towards the wall can be written. Here the first moment of the electron velocity $\langle v \rangle$ is used, calculated in equation 1.9 with the electron energy distribution function (EEDF) $f_e(v)$.

$$\langle v \rangle = \int_{\mathbb{R}} v \cdot f_e(v) dv \quad \Rightarrow \quad j_e = -\frac{e}{4} n_e \langle v \rangle \exp\left(-\frac{e\Delta\Phi}{k_B T_e}\right) \quad (1.9)$$

Impinging ions are neutralized by the free electron gas in the metal when they approach the surface of the solid. If a fast electron impacts on the wall, there is a chance for it to collide with electrons of the solid and to release a secondary electron from the surface. The *secondary electron emission* coefficient is defined as γ : one impinging electron emits γ electrons from the metal. This *SEE* reduces the $\Delta\Phi$ of the sheath potential because it creates an additional electron current from the wall towards the sheath edge, therefore altering the continuity condition $j_i = j_e$. A new *effective potential drop* $\Delta\Phi_{\text{eff}}$ can be derived in equation 1.10. There is a critical value γ_c where the wall potential gets unstable.

$$\Delta\Phi_{\text{eff}} = -\frac{k_B T_e}{e} \cdot \ln\left((1 - \gamma) \sqrt{\frac{m_i}{2\pi m_e}}\right) \quad (1.10)$$

Secondary Ion Emission Experimental results from [8] indicate that ions are produced near the surface of a metal electrode and heavily accelerated in the plasma sheath. In theory, secondary emission by surface ionization — in analogy to the surface neutralization — occurs with incident atoms of thermal energy. Hence one assumes a positively biased wall at high temperatures as the target. Its valence level is therefore broadened, giving an atom A the chance to deposit an electron at the metal. After equilibrating thermally, a positive ion is emitted by chance. This statistical process can be described by a thermodynamic equation (see equation 1.11) yielding the ionization coefficient of A . In equation 1.11 a modified approach for the *Saha-Langmuir equation* on the degree of ionization in gases can be found. Here, the surface temperature T and average work function $\bar{\Phi}_+$ are important quantities.

Additionally, the ionization energy $I(A)$ — or impact energy —, the particle fluxes of both species j and j^+ , corresponding statistical weights w , w^+ and reflection coefficients at the intrinsic potential barrier r/r^+ are used.

$$A \rightleftharpoons A^+ + e^-$$

$$\alpha^+(A^+) = \frac{j^+}{j} = \frac{(1-r^+)w^+}{(1-r)w} \cdot \exp\left(\frac{\bar{\Phi}_+ + e\sqrt{eV_{\text{ext}}} - I(A)}{k_B T}\right) \quad (1.11)$$

The Schottky term $e\sqrt{eV_{\text{ext}}}$ describes the reduction of the work function of electrons in a metal solid due to a large external electric field. At high temperatures of, e.g. 1000 K and applied voltages $V_{\text{ext}} < 1$ kV, this term and the corresponding internal reflection coefficients r/r^+ can be neglected — it appears to be just half of the thermal energy at room temperature. However, theoretical studies for such coefficients are missing.

In addition to SIE of positive ions, the model can be easily applied for negative ions with small changes to equation 1.11: a negatively biased electrode is assumed and the average work function yields a different sign. The electron affinity of the incident particle B is $A(B)$.

$$B + e^- \rightleftharpoons B^-$$

$$\alpha^-(B^-) = \frac{(1-r^-)w^-}{(1-r)w} \cdot \exp\left(\frac{-\bar{\Phi}_- + e\sqrt{eV_{\text{ext}}} + A(B)}{k_B T}\right) \quad (1.12)$$

Applying the former assumptions to both equations of positive and negative ions, inserting a homogeneous work function $\Phi = \bar{\Phi}_- = \bar{\Phi}_+$ for the used substrate yields the originally derived *Saha-Langmuir equations*.

$$\alpha^+(A^+) = \frac{w^+}{w} \exp\left(\frac{\Phi - I(A)}{k_B T}\right), \quad \alpha^-(B^-) = \frac{w^-}{w} \exp\left(\frac{-\Phi + A(B)}{k_B T}\right) \quad (1.13)$$

Though only considering atomic particles onto the wall, forms similar to equation 1.13 can also be derived for molecular surface interactions [7]. For conditions and materials of ccrf discharges no calculated reflection coefficients.

Works of, e.g. [18] and [10] investigated ion beam scattering, electron loss and transport in plasma sheath environments for metal walls, especially MgO(100) surfaces. There Ustaze et al. studied incident oxygen gas particles — ions and neutrals — on magnesium oxyde surfaces. Impinging atoms became negatively charged ions, picking up electrons from the MgO of the wall. This interaction, though requiring a minimum ionization and liberation energy for the electron, is most effective at low energies < 1 eV. This is due to a maximum of residence time at the target for an incoming atom. Hence it can be considered a non-resonant charge transfer process at the anion site. Further details can be found in [7].

Ions hitting onto the wall will result in an anion current in opposing direction:

$$j_- = \eta j_+, \quad (1.14)$$

with a corresponding efficiency of an incident positive particle η . The same stability criteria apply for η as they do for the electron emission coefficient γ . In case of SIE beyond a critical value η_c , a second plasma sheath may develop, enclosing the bulk and an inner sheath and reducing transport in-between.

1.1.4 Self Bias Voltage

An important step towards the electric characterization of ccrf discharges is the development of a replacement circuit, see figure 1.4. Thus, one can define a specific impedance for a rf discharge of excitation frequency ω . The value of ε_p resembles the permeability of the working gas between the driven and/or grounded electrode [12]. In addition, this volume has the capacity C_p — the capacity of a cubicle with a cross section A , thickness b and electron-neutral collision frequency $\nu_{e,n}$ calculates like equation 1.15.

$$\varepsilon_p = 1 - \frac{\omega_{p,e}^2}{\omega(\omega - i\nu_{e,n})}, \quad C_p = \varepsilon_p C_0 = \varepsilon_p \varepsilon_0 \frac{A}{b} \quad (1.15)$$

$$Z_p = \left(i\omega C_p + \frac{1}{\frac{1}{\omega_{p,e}^2 C_0}(\nu_{e,n} + i\omega)} \right)^{-1} \quad (1.16)$$

The equation 1.16 represents the full electrical impedance, consisting of the inverse sum of real and imaginary resistance, as well as the capacity of the neutral gas volume. Here, $i\omega/(\omega_{p,e}^2 C_0)$ characterizes the electrons inertia in regard to an external excitation ω . The real part $\nu_{e,n}/(\omega_{p,e}^2 C_0)$ denotes the resistance by neutral particle collisions. For high excitation frequencies, e.g. 13.56 MHz the bulk impedance can be neglected (see equation 1.16, [6]). Both sheath capacities of anode and cathode take the dominant part. Therefore, the discharge potential and voltage can be written as:

$$U(t) = U_{sb} + U_{rf} \sin(\omega t), \quad \Phi_p(t) = \overline{\Phi_p} + \Phi_{rf} \sin(\omega t). \quad (1.17)$$

Both sheaths of the electrodes collapse completely during a full cycle of $U_{rf}(t)$. Therefore no potential barrier is hindering the charged species to hit the electrodes. Electrons and ions can impinge on the surface and force the plasma potential Φ_p to level out with the walls. This short circuit between plasma and sheath occurs when Φ_p becomes negative with regard to the excitation. The equation 1.18 and figure 1.3 express this circumstance.

$$\Phi_{p,max} = \overline{\Phi_p} + \Phi_{rf} \geq U_{sb} + U_{rf}, \quad \Phi_{p,min} = \overline{\Phi_p} - \Phi_{rf} \geq 0 \quad (1.18)$$

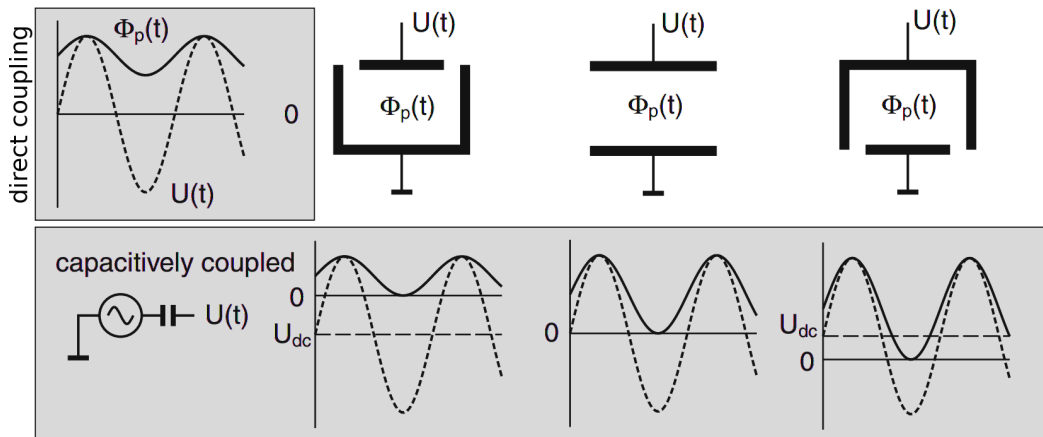


Figure 1.3: Schematics of the voltage $U(t)$ and plasma potential $\Phi(t)$ for a directly and capacitively coupled rf discharge. Different cases of symmetry are shown: enlarged driven electron, grounded electrode and a symmetric discharge. [12]

If there is no special coupling between electrode and electrical driver, the equality in equation 1.18 is true. However, if a capacitive coupling is used, there can not be any net current between excitation and electrode. The capacitance can not be inverted over the course of one rf cycle. The electron currents are then equal on both electrodes, therefore shifting the minimum plasma potential to ground and the maximum to the excitation. Finally, the dc *self bias* part U_{sb} and the mean plasma potential $\overline{\Phi_p}$ are

$$\overline{\Phi_p} = \frac{1}{2}(U_{sb} + U_{rf}),$$

$$U_{sb} = \frac{C_1 - C_2}{C_1 + C_2} U_{rf}. \quad (1.19)$$

If the excitation frequency ω is small compared to other time scales, e.g electron and ion plasma frequencies, the electron current from the sheath j_L becomes bigger than the displacement current j_{dc} . Hence the electron current onto the driven electrode decreases by a maxwellian factor — this is a function of the thereon applied voltage — compared to the corresponding ion current. Therefore the sheaths impedance is bigger than those of the floating walls. Together with equation 1.17 and equation 1.6 the plasma potential Φ_p vanishes and only the currents onto the driven electrode have to be equal. For small values of ω equation 1.20 yields the *self bias voltage* [12]. Here, I_0 denotes the zeroth order modified *Bessel function*.

$$U_{sb} = \frac{k_B T_e}{e} \ln \left[I_0 \left(\frac{e U_{rf}}{k_B T_e} \right) \right] \quad (1.20)$$

1.1.5 Dielectric Displacement Current

Due to their higher mobility and plasma frequency $\omega_{p,e}$, the electron distribution can follow an external excitation with a similarly high frequency much better than the heavier ions species. Because of that, one can assume those as nearly stationary, e.g. $\omega_{p,i} \ll \omega_{p,e}, \omega_{rf}$. Investigating the circumstances and consequences of this relation yields the displacement current j_d .

Let us suppose an area of thickness d in front of a negatively charged wall, where the electron density is negligible and the corresponding ion property constant at $n_{0,i}$. Thus an electric field of

$$E_0 = -en_{0,i}d/\varepsilon_0 \quad (1.21)$$

establishes. If the wall potential now decreases due to electron bombardment or external manipulation, the sheaths border moves further inside into the discharges volume with the velocity

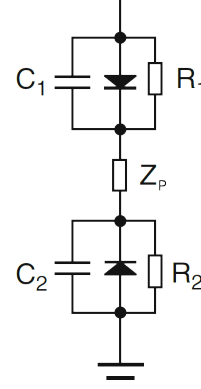


Figure 1.4: Replacement circuit of an asymmetrically driven ccrf discharge. [12] A diode represents the directed electron current from the sheaths $j = 1, 2$.

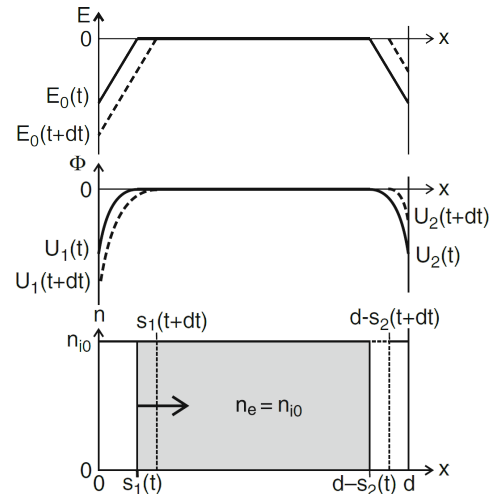


Figure 1.5: One dimensional density, potential and electric field for an asymmetric, harmonically driven discharge. Note the moving sheaths border. [12]

$u_s = ds_1/dt$. Thus, the sheath expansion and hence charge movement creates an additional *displacement current* j_d , which is compensated with $j_{d,e}$ the electron current from this border displacement. Hence charge conservation and continuity is satisfied [2].

$$j_d = -en_{0,i}u_s = -j_{d,e} \quad (1.22)$$

Electrons that are pushed out of this positive space-charge area then contribute to the plasma bulk density and to the quasi neutrality $n_e = n_{0,i}$. But in case of a harmonically driven discharge, the sheath in front of the opposing electrode is shrinking with $ds_1 = -ds_2$. Hence the spatial expansion and position of the bulk are oscillating sinusoidal, or: the sheaths thickness oscillates harmonically around a mean value, e.g. s_0 . The associated voltage drop across the discharge [12] between the sheath potentials $U_{1/2}$ is

$$\Delta U = U_1 - U_2 = -\frac{2en_{i,0}s_0}{\varepsilon_0} \exp(i\omega t) \quad (1.23)$$

1.1.6 Heating Mechanisms

Ohmic Heating In a spatially uniform electric field that oscillates perpendicular to the electrodes harmonically, like it is the case in the bulk of a ccrf discharge, electrons periodically gain and loose energy in the absence of collisions without any net energy gain [14]. This is due to the symmetrical de-/acceleration in the sheaths over one rf cycle. Let us assume the electric field have no or a negligible component parallel to the electrodes. Hence the mean absorbed power by the electrons in an oscillating electric field is

$$\overline{P}_{ohm} = \omega_{rf} \int_0^{T_{rf}} j_{tot}(t) \cdot E(t) dt \quad (1.24)$$

$$m_e \frac{dv_e}{dt} = -eE(t) - m_e \nu_{n,e} v_e \quad (1.25)$$

The total charge current density j_{tot} is the sum of displacement current from section 1.1.5 and conduction current $en_{e,0}v_e$. Solving equation 1.25 for the velocity, one obtains an imaginary and real part due to the bulks impedance, like it was discussed earlier in section 1.1.4. Substitution of this result [14] gives

$$\overline{P}_{ohm} = \frac{|E_0|^2 \text{Re}(\sigma_p)}{2} = \frac{|j_0|^2}{2 \text{Re}(\sigma_p)}, \quad \sigma_p = \frac{n_e e^2}{m_e(\nu_{n,e} + i\omega_p)} \quad (1.26)$$

This is, again, the total mean power dissipated into the electron species through acceleration in a harmonically oscillating electric field and neutral gas friction. The property σ_p is the plasma conductivity, hence resulting in $j_0 = \sigma_p E$. This demonstrates that power from an spatially uniform, harmonically oscillating electric field can only be transferred via collisions. Elastic electron-neutrals collision transferred into a direction perpendicular to the field and is, hence, not lost during the reversal of $E(t)$. Therefore the electron species gains energy during the field oscillation. This mechanism is called *ohmic heating* and takes place mainly in the plasma bulk.

Stochastic Heating Low-pressure, capacitively coupled rf plasma can be stabilized by collisionless heating in the sinusoidally modulated discharge sheaths, like it was proposed earlier in section 1.1.2.1. Most theoretical models assume a ‘hard wall’ approximation (HWA), where the electrons are considered to collide elastically with the oscillating sheath edge. Heating power

is then averaged by reverse and forward energy fluxes into and out of the sheath respectively. This gives an easy access to heating mechanisms of the proposed discharges.

The heating mechanism in such low pressure plasma is of particular importance, because collisions are rare and sheath processes are key to the sustainability of the discharge (see e.g section 1.1.3). The afore-mentioned HWA uses the '*fermi acceleration*' argument, which implies that the particles are heated or cooled due to the sheaths sinusoidal oscillation and a corresponding de-/acceleration. This process, though relying on enough randomization in phase-space inside the bulk, sufficiently creates a net heating of the plasma [4, 3]. This is referred to as *stochastic heating*.

Consider the sheaths electric field as constant, $E = U_{sb}/s_0$, the bulks expansion to be l and the sheaths thickness d being modulated cosinusoidal. The equation of motion for an electron in the sheath is taken from above, cancelling out the part of ohmic neutral gas heating.

$$d(t) \approx s_0 \left(1 + \frac{U_{rf}}{U_{sb}} \cos(\omega t) \right) \quad (1.27)$$

The equation 1.25 is introduced to be dimensionless with the substitution of the corresponding parameters: $\alpha = m_e \omega^2 s_0^2 / (e U_{sb})$, $\beta = U_{rf}/U_{sb}$ and $\epsilon = s_0/l$. Integration yields the velocity $\mu(\tau)$ of an electron as it moves through the sheath. The transit time τ is considered for one pass through the sheath of the particle. It can be used to calculate the change in velocity experienced by the electron on each bounce between this oscillating and a fixed wall — this would be the lowest order *fermi acceleration*. Assuming there are two distinct points in motion, where the particle enters (index n) and re-enters (index $n+1$) the sheath, this gives, using φ_n the phase of the sheath, for the transit time and velocity [3]

$$\tau_n \approx \frac{2\alpha(\mu_n - \beta \cos \varphi_n)}{1 + \alpha\beta \cos \varphi_n}, \quad \mu_{n+1} = -\mu_n + \frac{2(\mu_n - \beta \sin \varphi_n)}{1 + \alpha\beta \cos \varphi_n} \quad (1.28)$$

In *hamiltonian mappings*, those two variables are not canonically conjugate, hence insufficient for checking conserved quantities. One has to keep that in mind when evaluating the HWA approximation. The change in velocity in one pass through the sheath becomes the impulse approximation of the *Fermi acceleration*. Here, written again with common variables.

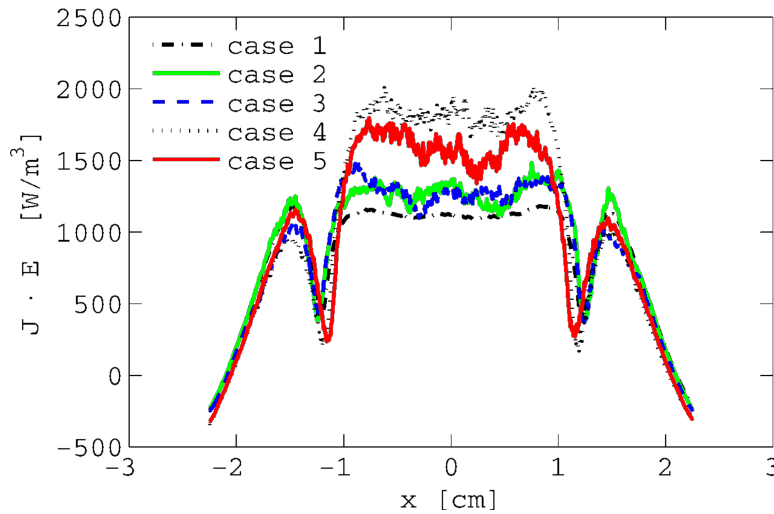


Figure 1.6: Electron heating rate for a ccrf discharge of parallel plates at 6.7 Pa with an electrode gap of 4.5 cm at 222 V. Other corresponding plasma parameters are noted in table 1.1. [5]

Case	Φ_0	$n_{e,0}/\text{m}^{-3}$	$n_{i-,0}/\text{m}^{-3}$	$n_{i+,0}/\text{m}^{-3}$	$T_{e,0}/\text{eV}$
1	101.30	2.43×10^{14}	1.17×10^{16}	1.20×10^{16}	2.83
2	101.25	2.29×10^{14}	1.21×10^{16}	1.23×10^{16}	2.98
3	101.75	2.18×10^{14}	1.19×10^{16}	1.20×10^{16}	2.98
4	103.11	1.55×10^{14}	1.75×10^{16}	1.78×10^{16}	3.59
5	102.55	1.65×10^{14}	1.70×10^{16}	1.71×10^{16}	3.43

Table 1.1: Selected plasma parameters for the used cases in figure 1.6 at the center of the discharge. [5]

$$\Delta v = v_{n+1} - v_n = -2\omega s_0 \frac{U_{\text{rf}}}{U_{\text{sb}}} \sin \varphi_n \quad (1.29)$$

A question to answer is what parameter defines the degree of randomization required for an ample stochastic heating in the plasma sheath. Therefore, K is defined as a function of phase-space chaos by electron energy. Additionally, a simple condition for stochastic motion is derived at the same time.

$$K = \alpha \beta \frac{U_{\text{sb}}}{\epsilon E}, \quad E < m_e \omega^2 s_0 l \frac{U_{\text{rf}}}{U_{\text{sb}}} \quad (1.30)$$

As is well known [3], chaotic motion occurs in this mapping for $K > 1$. It decreases with increasing energy, so the system is less stochastic at higher energies. This is due to the shrinking phase shift across the discharge volume with higher energies. Hence phase correlations between successive collisions in and with the plasma sheath reduce stochasticity.

Last, but not least, one calculates the instantaneous power dissipated into the plasma due to this heating mechanism. Here, using the sheath speed from above u_s , the electron drift velocity u_e and the maxwellian electron velocity distribution function $f_v(v_e, t)$, Lieberman [9] finds

$$P_{\text{stoc}}(t) = -2m_e \int_{u_s}^{\text{inf}} u_s(v_e - u_s)^2 f_v(v_e, t) dv = 2n_{e,0} u_e k_B T_e \sin(\omega t) \quad (1.31)$$

Clearly, this results yields not net heating if averaged over one rf cycle. That is, if the current used would be conserved in a manner the HWA is predicting it, or the electron drift velocity does not satisfy the maxwellian distribution function. Hence, there have to be deviations from the proposed theory of stochastic heating. This would be e.g. ab initio information about the EEDF, unconsidered transit time effects of the sheath electric field and neglected particle losses and current conservation.

There are more theoretical approaches on the heating in low-pressure, low-temperature rf plasma. For example, Surendra et al [15] put forth the idea that the compression and decompression of the electron density volume between opposing plasma sheaths generates heat inside the bulk is responsible for the observed heating.

The electron heating profile is shown in figure 1.6. The electron heating peaks near the sheath edges are due to the stochastic heating while the main plateau in the bulk is a result of the dominantly strong ohmic heating with slow electrons and neutral gas friction.

1.2 Oxygen Plasma Chemistry

In comparison to most inert working gases in ccrf discharges, oxygen has an overwhelming number of reaction sets for collisions of elastic, inelastic and reactive character. Additionally, the negative ion species has to be taken into account when discussing collisional processes. For example, an in-depth benchmarking of both simulated and experimentally measured cross section data is given by Gudmundsson et al. in [5]. There, 33 collisions and reactions have been revisited, already reducing the investigation to the most important processes in ccrf plasma. In this thesis the selection of possible reactions will be based on [1] and slightly modified. The final collection of cross sections can be found in table 1.2 and observed in figure 1.7. Those data are semi-empirical, meaning part of them are based on measurements in finite energy ranges and low-/high-energy asymptotic models. Cross sections for very high energies are not important, as the collision probability usually decays very fast here.

As already seen in section 1.1.6, collisions strongly influence the particle distribution functions and density profiles. Furthermore, a good understanding of the plasma chemistry is key to, e.g. applications in surface physics supported by gas discharges. Of high importance for plasma-assisted material processes is the generation of negative ions. Hence the ratio $\alpha = n_{i,-}/n_e$ is important to characterize the electronegative plasma, like a ccrf oxygen discharge by $\alpha > 1$.

I will highlight the most important collisions and reactions in the following section.

Nr.	Reaction	Type
Elastic scattering		Energy loss
(1)	$e^- + O_2 \rightarrow O_2 + e^-$	
(2)	$O^- + O_2 \rightarrow O_2 + O^-$	
(3)	$O_2^- + O_2 \rightarrow O_2 + O_2^-$	
Electron energy loss scattering		Energy loss
(4)	$e^- + O_2 \rightarrow O_2^\nu + e^-$	Vibrational excitation ($\nu = 1, \dots, 4$)
(5)	$e^- + O_2 \rightarrow O_2(Ryd) + e^-$	Rydberg excitation
(6)	$e^- + O_2 \rightarrow O(1D) + O(3P) + e^-$	Dissociative excitation at 8.6 eV
(7)	$e^- + O_2 \rightarrow O_2(a^1\Delta_g, b^1\Sigma_g)$	Meta-stable excitaion
Electron and ion reactions		Creation and loss
(8)	$e^- + O_2^+ \rightarrow 2O$	Dissociative recombination
(9)	$O^- + O_2^+ \rightarrow O_2 + O$	Neutralization
(10)	$e^- + O_2 \rightarrow O + O^-$	Dissociative attachment
(11)	$O^- + O_2 \rightarrow O + O_2 + e$	Direct detachment
(12)	$e^- + O_2 \rightarrow 2e^- + O_2^+$	Impact ionization
(13)	$e^- + O^- \rightarrow O + 2e^-$	Impact detachment

Table 1.2: Most important collision and reactions in ccrf plasmas. Empirical and simulated data, which have been included in this simulation are shown in figure 1.7.

1.2.1 Collisions and Reactions

Elastic Scattering The elastic collisions of (1)–(3) conserve the particle numbers. Those are inter-species scattering processes, which will be assumed to have an isotropic incident angle dependency [1]. Intra-species elastic collisions were not very important at the selected parameter regions, though ion-ion scattering can strongly influence the IEDF structure of the concerned densities are very high. However, for the electron species a binary *coulomb scattering* process was used: the scattering angle χ is given by equation 1.32 with v_{rel} the relative velocity, $\ln \Gamma$ the Coulomb logarithm (see table A.1) and τ_c the collision time.

$$\langle \tan^2 \frac{\chi}{2} \rangle = \frac{e^4 n_e \ln \Gamma}{8\pi \epsilon_0 m_e^2 v_{\text{rel}}^3} \tau_c \quad (1.32)$$

The figure 1.7 shows the corresponding cross sections. In fact, only two are elastic processes, where as the collision of O_2^+ and the neutral molecule is a charge exchange reaction with momentum transfer. This kind of process:



is important for the consideration of surface effects. An ion with greater than thermal velocity coming from the wall will be cooled down by charge exchange collisions, which will transfer heat into the neutral reservoir.

Electron Energy Loss Electron energy loss occurs due to inelastic collisions (4)–(7), where an oxygen molecule is excited or dissociated into fragments. Here, the spatio-temporal evolution of the molecule or the fragments are of no interest for this thesis. Hence they are treated as ‘test collisions’, in which only the electrons lose momentum and change direction. Again, the neutral particle reservoir is considered to equilibrate at a sufficiently short time scale $< 10^{-15}$ s. Rotational excitations are found to be unimportant, though the vibrational parts considerably influence the EEDF [5]. The isotropic post-collision relative velocity change in the center-of-mass system gives

$$\tilde{v}_{\text{rel}} = \sqrt{v_{\text{rel}}^2 - \frac{2\Delta E}{\mu_{i,j}}}. \quad (1.34)$$

The most important electron energy loss scattering is the vibrational and electronic excitation, as well as the dissociation of the oxygen molecule.

Electron and Ion Channels The last class of collisions concerned here are the electron and ion production processes. Collisions (8) and (9) are the annihilation of the two oppositely charge particles. Those are namely recombination processes. The ion-ion neutralization is constructed by a *Landau-Zener* model, where the adiabatic energy of the (O^-, O_2^+) configuration decreases when the particles approach each other. At the critical distance R_c this energy drops below the one of the (O, O_2) configuration, yielding the probability to change states $\sigma_r(E)$

$$\sigma_r(E) = 4\pi R_c^2 \left(1 + \frac{1}{R_c E} \right). \quad (1.35)$$

The dissociative attachment (10) and direct detachment (11) are treated as binary collisions, like the elastic electron scatter process. For the dissociative attachment from the ground state

oxygen molecule a threshold energy of 4.2 eV is needed. The incident electron loses this energy to the O_2^- , which afterwards breaks up into the two fragments. The electron transition time is, again, assumed to be short on a nuclear timescale and the resulting particles share the remaining kinetic energy of the incident electron.

In the experiment there is a second stage for the direct detachment process: through associative detachment, oxygen atom, electron and molecule form an ozone O_3 particle. This most likely due to the presence of meta-stable $O_2(a^1\Delta_g)$. After the necessary threshold energy of 1.3 eV has been supplied to directly detach O^- on an oxygen molecule, the afore-mentioned detachment takes no energy whatsoever, making it a potentially important loss channel for cold O^- ions. For impact ionization (12) and detachment (13) the following is assumed: first, an inelastic binary collision takes place, in which the electron loses the necessary reaction energy. The post-collision oxygen particle is afterwards split into an additional e^- and atom/ion (O^-/O), which proceed to perform an elastic binary collision. During this process, energy and momentum conservation is satisfied, ensuring numerical stability.

1.2.2 Anion Species

The main production channel of negative oxygen ions in ccrf discharges at low pressures and temperatures is the dissociative attachment reaction (10). Here, an electron becomes attached to a molecule. The successive electronic excitation is of short duration and does not change the intra-molecular distance. Afterwards, there is a significant chance of transition to a dissociative state exists, which has a lower equilibrium energy at greater intra-nuclear distances. Hence,

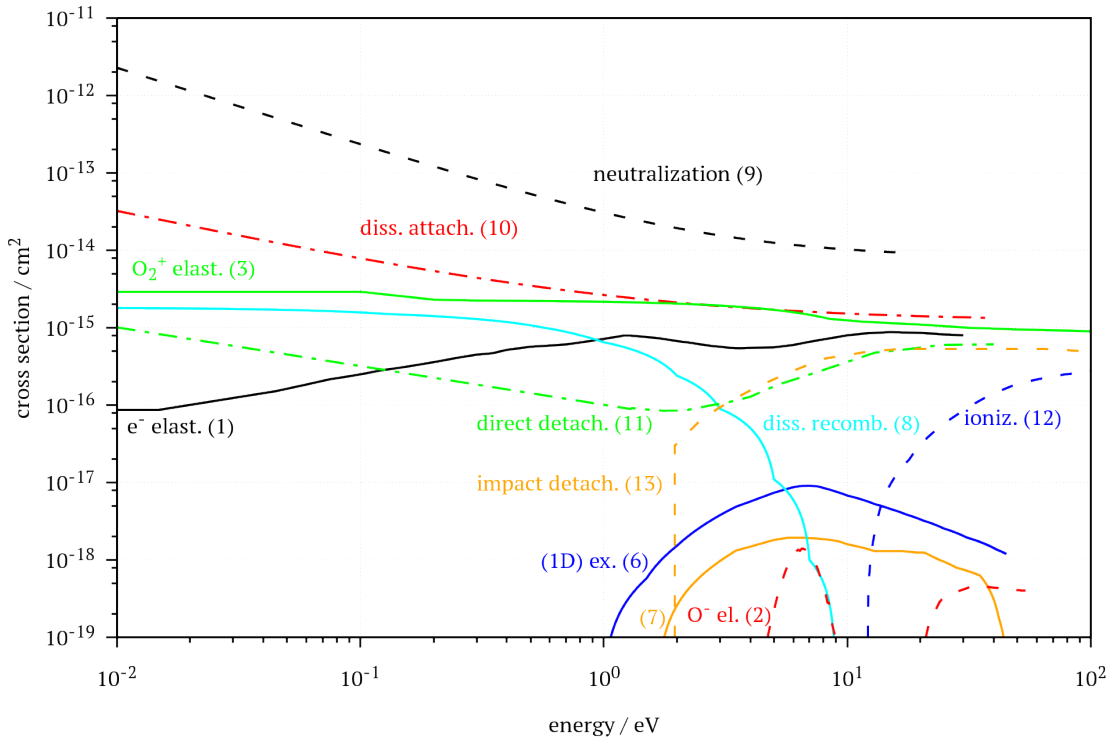


Figure 1.7: Cross section data of electron energy loss, electron and ion production/loss and elastic scattering collisions from [5] and [1]. The corresponding reaction equations are shown in table 1.2.

the dissociation of this molecule is rather likely.



Another possible creation channel is a three-body collision of non-dissociative character, whose cross sections is magnitudes smaller than the one of equation 1.36. Hence I will only consider dissociative attachment reactions (10) for the anion production.

Negative ion loss can happen through reactions (11), (13) and (9). The latter is the only collision with a cross section larger than the creation via dissociative attachment (see figure 1.7). For all relative energies, the neutralization has a probability of at least one magnitude larger than the other channels. Cross sections of direct (11) and impact (13) detachment are, depending on the energy, about one to two orders of scale smaller.

In general, the produced negative ions are cold. The anion distribution reaches until the boundaries of the bulk, where processes with large cross sections at low energies become important [1]. Those reactions would be ion-ion neutralization and associative detachment. Direct detachment, though being still present around $E < 1$ eV, has an energy threshold and is not significant for this region. Furthermore, the probability of neutralization (9) is proportional to the O_2^+ -density. Bronold et al. proposes, that the production and loss of O^- is rather insensitive to voltage changes up to 300 V. Furthermore, the most important range for incident energies will be 4–15 eV, while the EEDF is rather voltage-independent.

Considering the physics of a negative ion — O^- follows the same dynamic and kinetic behaviour as the electrons, but is easily confined by the plasma potential due to their much greater mass and, hence $\omega_{p,i} \ll \omega_{p,e}$ — the main loss and production channels are most prominent in the bulk. Therefore, a low-pressure, low-temperature ccrf discharge has an electronegative core, in which the cold anions are captured, and areas where they are excluded. The presence of negative ions also has a great impact on the distribution functions of other plasma species. It is possible to form a quasi-neutral volume core, consisting only of ion species, and a peripheral electron-ion plasma in the discharge sheaths. At pressures > 30 Pa and large input powers, the value of electronegativity α leads to instabilities between ionization and electron attachment reactions. The electron density peaks, where as the corresponding temperatures drops. Because of the strong negative ion coupling, the O^- density fluctuates as well.

1.3 Particle-in-Cell Simulations with Monte Carlo-Collisions

Particle-In-Cell simulations with Monte-Carlo-Collisions (PIC-MCC) represent a powerful tool for fully kinetic, high-dimensional plasma studies, with inclusion of complicated reaction/collision routines, as well as field solving methods. Hence they are used in all branches of plasma physics, ranging from simple laboratory discharges to electro-propulsion ion-thrusters and interplanetary astrophysical system. This kind of computer code simulates the motion of up to 10^{10} pseudo-particles, though this limit is only due to the available fast cache memory on the system side, in a continuous 1d3v-/2d3v phase-space. Macro-quantities like forces, fields and densities are stored and calculated on a strict mesh scheme with fixed intervals. The computational cost sums up to $N \log(N)$ per timestep — with N the total particle number — because the self-consistent electrostatic macro-fields are calculated globally by the *Poisson's equation*, and no particle-particle interactions are considered.

In the following section the motivation and basic scheme of a PIC-MCC simulation will be highlighted. Accordingly, the collision routines will be layed out, as well as the transition from a 1d3v to 2d3v model. As it was mentioned in chapter 1, the focus of this thesis is on unmagnetized plasmas. The magnetic field generated from the moving charged particles is small enough that the force of $q_j(\vec{v}_j \times \vec{B})$ is negligible in comparison to $q_j \vec{E}$.

1.3.1 Principles

In general, the spatio-temporal evolution of the velocity distribution function $f_j(\vec{v}, \vec{r}, t)$ is given by the *Boltzmann equation*:

$$\frac{\partial f_j}{\partial t} + \vec{v} \cdot \nabla_{\vec{r}} f_j + \frac{q_j}{m_j} \vec{E} \cdot \nabla_{\vec{v}} f_j = \left(\frac{\partial f_j}{\partial t} \right)_{\text{Coll}}. \quad (1.37)$$

In this equation, the product of $q_j \vec{E}/m_j$ denotes the electrostatic force onto the particle of species j . The velocity and space gradient are calculated like $\nabla_{\vec{r}} f_j = \partial f_j / \partial x \cdot \vec{e}_x + \dots$ and so on. The right hand side of $(\partial f_j / \partial t)_{\text{Coll}}$ is the sum of all collisional effects on $f_j(\vec{v}, \vec{r}, t)$. An approach would be an integral form, in which all probabilities of a two-body interactions with different incident and outgoing velocities are summed up in a convolution integral with $f_j(\vec{v}, \vec{r}, t)$.

The approach via the distribution function yields the advantage of an easy access to the aforementioned macro-quantities, the zeroth and first moment are noted below in equation 1.38. Using the moments, one can write down $f_j(\vec{v}, \vec{r}, t)$ at a thermodynamical equilibrium of $T_{j,0}$ as the *Maxwell-Boltzmann-distribution-function* in equation 1.39.

$$n_j(\vec{r}, t) = q_j \int_{-\infty}^{\infty} f_j(\vec{v}, \vec{r}, t) d\vec{v}, \quad \langle v_j(\vec{r}, t) \rangle = \frac{1}{n_j(\vec{r}, t)} \int_{-\infty}^{\infty} \vec{v} f_j(\vec{v}, \vec{r}, t) d\vec{v} \quad (1.38)$$

$$f_j(\vec{v}, \vec{r}, t) = \frac{n_j(\vec{r}, t)}{q_j} \hat{f}_j(\vec{v}, \vec{r}, t) = \frac{n_j(\vec{r}, t)}{q_j} \left(\frac{m_j}{2\pi k_B T_{j,0}} \right)^{3/2} \exp \left(-\frac{|\vec{v}_j|^2}{v_{j,\text{th}}^2} \right) \quad (1.39)$$

In a Maxwellian plasma at equilibrium, one could use a fluid dynamic approach, where the equations of motion for a single particle are multiplied with the number density function. This would reduce the computational cost drastically, as one would no longer have to track each particle individually, and sufficiently describe the discharge by characterization of macro-quantities. This is true, if mean-free-paths are small and collisions rather likely, hence the afore-mentioned distribution function correct. In a low-temperature, low-pressure ccrf discharge mean-free-paths are large and collisions happen infrequently, which is why a Particle-in-Cell simulation method is used.

Satisfying the above requirements, the n -th equation of motion in the N -particle system becomes:

$$\frac{d\vec{x}_n}{dt} = \vec{v}_n, \quad \frac{d\vec{v}_n}{dt} = \frac{1}{m_n} \vec{F}_{n,L}(\vec{x}_n, \vec{E}, t) = \frac{q_n}{m_n} \vec{E}(\vec{x}_n, t) \quad (1.40)$$

where $F_{n,L}$ is the *electrostatic Lorentz force*.

First, the global charge density is calculated by interpolating the point charges q_n of each particle onto the afore-mentioned fixed mesh grid (equation 1.41). Next, the Poisson's equation is solved globally on that grid (equation 1.42), using the interpolated density. At last, the

Maxwell's equation 1.43 yields the electric field.

$$\rho(\vec{r}, t) = \rho(\vec{x}_1, \vec{x}_2, \dots, \vec{x}_N, t) \quad (1.41)$$

$$\Rightarrow \Delta\Phi(\vec{r}, t) = -\frac{\rho(\vec{r}, t)}{\varepsilon_0} \quad (1.42)$$

$$\Rightarrow \vec{E}(\vec{r}, t) = -\nabla\Phi(\vec{r}, t) \quad (1.43)$$

The number of N is of orders of magnitude higher than what the best supercomputers can handle. Hence it is assumed that one simulated particle at \vec{x}_n and velocity \vec{v}_n represents many physical particles. This *superparticle factor* is usually between 10^3 – 10^4 , depending on the size and initial density in the simulated domain. Those superparticles follow the same dynamic and kinetic behaviour like their physical counterparts, assuming that all other relevant parameters are scaled accordingly.

Like the domain composition and field mesh grid, the time is divided into discrete time steps, which yields the simulation time $t \rightarrow t_k = t_0 + k \Delta t$ (and correspondingly all other physical properties). Here, a *leap frog* method is used to calculate the velocities, in contrast to other time-dependent attributes, which still satisfies the needs of accuracy, short computational times and stability. With each calculation step, the error scales with $\sim \Delta t^2$ and fulfills the requirement for numerical stability $\Delta t^{\alpha > 1}$. The explicit leap frog solution is calculated with old quantities of the previous timestep, thus it is simpler and faster. The single drawback on this method would be the requirement of a smaller timestep, e.g. $\Delta t/2$.

The most significant part of the simulation code is the *particle mover* or *particle pusher*, in which the equation of motions are discretised and the new positions and velocities calculated. For each particle of index n and species j the following equations have to be solved at a given time step k , or $k + \frac{1}{2}$ respectively:

$$\vec{u}_{n,+} = \vec{v}_{n,k-1/2} + h \cdot \vec{E}_k, \quad h = \frac{q_j}{2m_j}$$

$\vec{x}_{n,k+1} = \vec{x}_{n,k} + \Delta t \vec{v}_{n,k+1/2} \quad \text{and} \quad \vec{v}_{n,k-1/2} = \vec{u}_{n,+} + h \cdot \vec{E}_k$

(1.44)

The field, potential and density only have to be calculated once per time step. Though this requires less effort, the calculation of \vec{E} , Φ and ρ need to be done by one processing core. The equation 1.41 and following are solved globally. For example, the Poisson's equation for a two-dimensional, with Δr equally grided mesh at $(r_1^{(1)}, r_m^{(2)})$ in a discrete form becomes the *five point star equation*:

$$4\Phi_{l,m} - \Phi_{l-1,m} - \Phi_{l+1,m} - \Phi_{l,m-1} - \Phi_{l,m+1} = \Delta r^2 \cdot \frac{\rho_{l,m}}{\varepsilon_0} \quad (1.45)$$

While the updated field, potential and density are calculated, all but one processing core remain idle and wait for the result to be distributed and used in the particle pusher in equation 1.44. The universal stability criteria for a kinetic plasma simulation using a PIC method with a twodimensional, spatial mesh size Δr and time step Δt are given by equation 1.46. The spatial and temporal step width should sufficiently resolve the smallest and fastest processes in the simulated model. Hence the physical scales of electron plasma frequency $\omega_{p,e}$ and Debye length λ_D are chosen. For example, an electron never flies beyond one Debye cell during a single step of time. Also the interpolation of the macro-quantities yields an error the size of micro-fluctuations

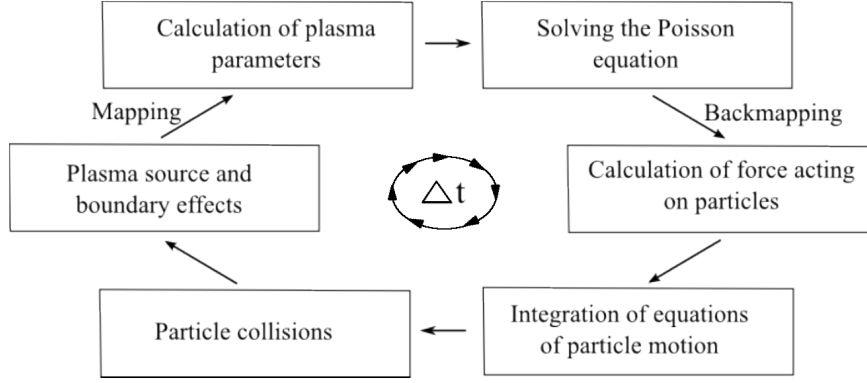


Figure 1.8: PIC simulation scheme [11]. The code starts with the initialisation of all particle species with their corresponding velocities and a first mapping process, followed by the solution of the Maxwell's equation equation 1.43. Afterwards the main loop with push, collisions, mapping and so on begins.

between single particles, thus is negligible.

$$\boxed{\Delta t_0 \leq 0.2 \cdot \omega_{p,e} \quad \text{and} \quad \Delta r_0 \leq 0.5 \cdot \lambda_D} \quad (1.46)$$

To summarize this section, a basic simulation code cycle for one time step of a PIC-MCC method is shown in figure 1.8. A more versatile and in-depth approach on PIC or Cloud-In-Cell (CIC) simulations can be found in [16].

1.3.2 2d3v PIC

In the following, I will highlight the difficult tasks of a spatially twodimensional PIC simulation, referring to the scheme in figure 1.8.

Discharge Setup In the beginning of the simulation, before the first calculation step is done, the domain has to be constructed. The cylindrical setup is reduced to the radial and axial dimensions, e.g. (r, z) for reasons of symmetry. The five-dimensional phase-space is completed with the full velocity triplet $\vec{v} = (v_r, v_z, v_\theta)$. Two onedimensional grids in radial and axial directions, with N_r and N_z equally sized partitions respectively, are layered over each other to form the final discharge domain. Hence, the area of a single mesh cell is Δr_0^2 . The spatial and temporal discretisation Δr_0 and Δt_0 are chosen to be dimensionless, so calculations inside the code can be performed much more easily and are less likely to have errors.

Additionally, certain physical properties have to be scaled according to the spatial weight of a cell. Because a ‘quasi-three-dimensional’ cell of coordinates (n_r, n_z) grows in volume with increasing radial index (for a more visual approach, take a look at figure 3.2), a weighting factor needs to be multiplied with properties like densities and pressure.

After the domain composition, the particle initialization is to be done. Here, one uses pressure and initial density to model a global distribution of electrons, ion and neutral species. The corresponding super particle factor is used to decrease computational time. Though it has been proven that this does not introduce artifacts to the simulations results — the equation of motion only depends on a charge-to-mass-ratio — it should not be too high. Collisions may be underrepresented when there are not enough targets, though in reality $\sim 10^4$ times the amount of particles would be available.

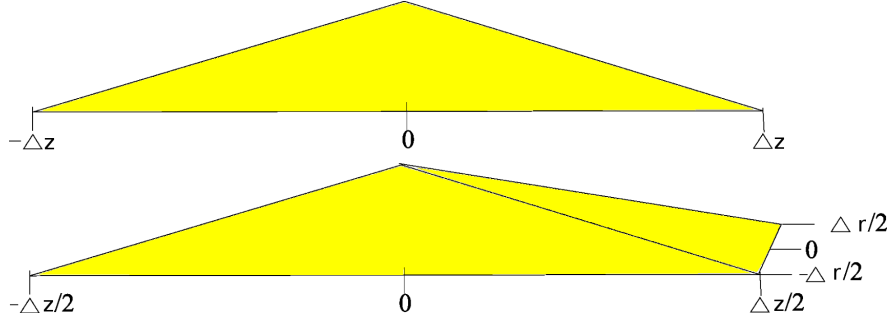


Figure 1.9: Linear weighting scheme for (top) 1D and (bottom) 2D simulations. The latter is an expansion into the radial dimension from a 1D case. The twodimensional approximation is called Cloud-In-Cell (CIC).

To initialize the particles, a number of electrons, ions and neutrals is distributed in each cell, using a Maxwell-distribution-function. Inside one mesh unit the, e.g neutrals are spread continuously and randomized. The same goes for the velocity, which is specified by the distribution function. The radial deformation of each cell has to be taken into account here. Therefore more particles have to be initiated in cells the closer they get to the outer limit of the cylindrical domain. Now that N particles have been distributed equally in the simulated area, the computational workload is shared between the M_{PC} processing cores. The domain is therefore decomposed in partitions of equal particle numbers, e.g N/M_{PC} . This speeds up the collisional and diagnostics routines, as each core only has to calculate on its own, but it does not reduce the time needed for the Maxwell's and Poisson's equation (see section 1.3.1).

Potential and Field Calculation After the domain is filled and decomposed, the resulting density distribution, potential and electric field have to be calculated. The charges need to be mapped to the grid points to generate a density, which can be used by a discrete solver of the Poisson's equation (see equation 1.45). A linear weighting function is applied for each charge to form the density. The resulting scheme for a particle at (r, z) in one and two dimensions is shown in figure 1.9 and equation 1.48. The index tuple k, j denotes the position in the twodimensional mesh, $n_{k,j}$ the corresponding density, (r_k, z_j) the position — this e.g would be $r_k = \Delta r_0 \cdot k$ and so on — and $S_{k,j}$ the statistical weight, composed of dimensionless charge, super particle and volume factor. The quotient $A_{k,j} = \Delta r_0^2$ normalizes the result, so that no error is made when summarizing all four contributions of a single particle to the density.

$$\text{1D:} \quad n_j = \frac{S_j}{\Delta z} (z_j - z) \quad (1.47)$$

$$\text{2D:} \quad n_{k,j} = \frac{S_{k,j}}{A_{k,j}^2} (r_{k+1} - r) \cdot (z_{j+1} - z) \quad (1.48)$$

To avoid possible self-forces and satisfy the conservation of momentum, the same weighting method has to be used when back-mapping the calculated forces from the discrete grid points to the particle positions. Again, for a more detailed discussion see [16].

The discrete matrix equation 1.45, and equation 1.42 respectively, are solved using a *LU-factorization*. Another matrix-solver for example would be the successive-over-relaxation method (SOR). The potential is calculated on every time step using this factorization, but the latter is done only once at the beginning, because it only depends on the mesh, and hence the composition of the matrix $\Phi \in \mathbb{R}^{N_r \times N_z}$. At this is point any potential boundary conditions, such as

external voltages $U_{rf}(t)$ or ground $\Phi = 0$ are applied to the result of Φ .

The calculated force from equation 1.43 is again mapped back to the individual particle positions using the same scheme as equation 1.48 for the two-dimensional mesh. Therefore, momentum and energy conservation is satisfied.

The resulting field and potential are distributed to all processing cores afterwards. The following routines are exercised on the corresponding domain partitions in parallel, which shares the computational burden and a lot of calculation time.

Particle Pusher The force acting on the particles is used in the N equations of motion from equation 1.44. This method is called *Boris algorithm*. The particle n is pushed, according to the calculated velocity $v_{n,k+1/2}$ and previous position $x_{n,k}$, to its new positions $x_{n,k+1}$. We will only consider the movement of charged species. A neutral push is not necessary, because the distribution of the neutral gas reservoir can be considered homogeneous due to their very large mean free path of $\sim 2 - 30$ cm, depending on the pressure.

Because we know that the electrons are the fastest species in the discharge, and the time step is chosen to sufficiently describe all plasma processes, one can significantly save computation time when pushing the slower species less often. Therefore a subcycling routine is written, which pushes the heavier and slower ions only every few steps, e.g 2-6 code cycles. The subcycling factor is sensitive to the species velocities, because the particles should not be pushed further than one Debye length λ_D to avoid numerical problems. The subcycling method is also applied to the collisional routine, which again saves more computational time.

After all velocities have been calculated and the particles are pushed, boundary conditions such as secondary emission, reflection and absorption at the walls are applied. Those processes are in general far from trivial. Therefore a *Monte-Carlo* algorithm is used, in which a random generated number $R \in [0,1]$ is compared with the probability $P(\theta, E)$ of a corresponding physical process, e.g. secondary emission. This probability is a function of incident angle θ and energy E . For $P > R$ the secondary particle of species j is injected with a given velocity distribution $f_j^{sec}(\vec{v})$, other wise the projectile is just lost (see section 1.1.3.1 and section 1.2).

Collision Routines The importance of collisions in ccrf discharges has been discussed earlier in section 1.1.6 and section 1.2.1. Therefore the collision routine should not be neglected.

In contrast to a global method, which calculates every single of the N^2 particle-particle interactions, the binary collision model is used. In this algorithm only particles from the same Debye cell are considered to collide with each other. Because self-forces were excluded from the simulation by the weighting scheme in the previous section, the inter-particle forces inside grid cells are underestimated. This can partially be compensated when introducing Coulomb collisions of charged particles using the binary collision operator. This still satisfies energy and momentum conservation and is sufficiently accurate [17]. Therefore random pairs of charges are chosen from a cell, so each particle has a single partner. This pair then is statistically collided using the simple approach from above of the boundary conditions.

For charged-neutral collisions the classical *Monte-Carlo-Collisions* simulation method is used: let us assume the collision probability

$$P(t) = 1 - \exp(-\nu_{n,j}) . \quad (1.49)$$

Here $\nu_{n,j} = \sum_{i=1}^I \nu_{n,j}^{(i)}$ is the collision frequency of neutrals and species j as the sum of all possible collisions. A single frequency is a function of $\nu^{(i)} = \sigma_i(v_{\text{rel}})n_i$ collision cross-section, density and relative velocity. The same algorithm is used to find charged-neutral pairs. The corresponding cross-sections at given relative velocities are shown in section 1.2.1.

1.3.3 Monte Carlo-Collisions

Chapter 2

Validation of Simulation by 1d comparison

2.1 Axial density profiles

2.2 Velocity and energy distributions

2.3 Transition to 2d simulation

Chapter 3

Simulation of capacitively coupled rf discharges

3.1 Experimental setup

After introducing the basics physics in section 1.1.3.1 and validating the code successfully in chapter 2, the effects of highly energetic negative oxygen ions can now be further investigated with the code.

3.1.1 Reference Discharge

Here, the referenced experiment was used by Küllig et al. [8] and Scheuer [13], and consists of a cylindrical setup, filled with oxygen at low pressures and gas flow rates (see figure 3.1). The stainless steel vacuum chamber had a diameter and height of 40 cm respectively and was filled with the process gas oxygen (O_2) at 5 sccm (**FC**). The discharge configuration consisted of an electrode in the center with 10 cm of diameter and a rf generator, constantly operating at a

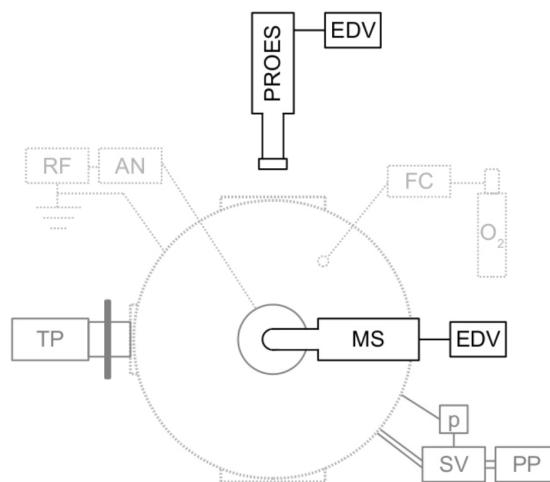


Figure 3.1: Top-down view schematic of the experiment [13], [8]. Shown is the setup without microwave interferometer, like it was used by Küllig et al.

frequency of 13,56 MHz and power outputs between 5 and 150 W (**RF** and **AN**), leading to applied voltages in the range of 100–1500 V. Shielding and discharge enclosure/chamber walls were grounded, therefore yielding a large area ratio between driven and grounded electrode and establishing a heavily asymmetric plasma. In addition, the powered electrode was coupled capacitively with the external generator, emphasizing the effect of the, in section 1.1.4 introduced self bias voltage. The value of U_{sb} ranged, depending on power output and discharge pressure, from -100 up to 500 V. In [8] the experiment was pulsed with short discharges at a frequency of 10 Hz. Line integrated measurements resulted in an average electron density of around 10^{11} – 10^{12} cm $^{-3}$. Showing a schematic top-down view of the experiment is figure 3.1. Here, the large ratio between driven and grounded parts is very well visualized. Hence, in later simulations it will be of sufficient accuracy to restrain the virtualized volume to a smaller setup.

The figure below includes further diagnostics like a mass spectrometer (**MS**) and phase resolved optical emission spectroscopy (**PROES**). The latter measured the mentioned densities via line integration across the plasma volume. The MS is a key instrument for the investigation pursued in this thesis, as it also measures species counts with respect to their contribution to their corresponding energy distribution function. For example, the ions created via secondary processes in the discharge sheath are accelerated towards the bulk and thus get into the MS with their characteristic speeds and mass. A significant increase of electron density was found for rf powers larger than 50 W or -220 V self bias voltage [8]. This led to a correlating negative oxygen ion density reduction and decrease of the electronegativity ratio $\bar{n}_{i,-}/\bar{n}_e$ from 4 to 0,03. During a different operation mode — called α -mode, contrary to the afore-mentioned γ -mode — at less than 50 V output power, electronegativity rises again, as well as the electron temperature T_e , yielding higher rate coefficients for, e.g. dissociative electron attachment and the alike. See section 1.2.2 for a more detailed approach.

3.1.2 Simulated Discharge

All of the above conditions are sufficient for a practical approach at a laboratory ccrf discharge with great repeatability. Though being highly optimized and developed over the course of many years, the twodimensional particle-in-cell code outlined above does not provide the tools and performance to feasibly simulate such large areas and particle numbers. Hence, one will reside to reducing the numerical expense by virtualizing smaller discharge areas and average densities, while trying to satisfy the same physical processes exhibited in [8].

The afore-mentioned 2d3v PIC code is used to simulated the referenced experiment. The spatial dimensions will be the radial component r and axial coordinate z . The geometry and simulation is optimized for cylindrically symmetric gas discharges.

To represent the strong asymmetry between driven and grounded wall areas, the sizes of anode, cathode and grounded chamber parts have been choosing accordingly. The experimental values for the self bias voltage U_{sb} were used to create a dc offset on-top of the rf voltage U_{rf} at the cathode. The domain composition with cells of width $\lambda_{D,e}/2$ (see section 1.3.1) makes it even more difficult to appropriately model the system. Hence a smaller discharge volume of a 4,5 cm radius and an electrode gap of 2,5 cm will be simulated. This usually leads to cell counts up to $2 \cdot 10^5$, which is small in comparison to the ‘real’ experiment, which would have to be covered by over 10^6 cells. Furthermore, the numerical expense grows with $N \log(N)$, and N being the particle number inside the cells (see section 1.3).

One has chosen pressures between 2 Pa and 10 Pa, with the possibility of changing it later during

number or location. Though collision routines are still exercised, the corresponding push of the neutral species is skipped.

3.2 Simulated ccrf Oxygen Discharge

In the collection of ?? twodimensional densities and potential are shown. Again, parameters were chosen as $U_{\text{rf}} = 400 \text{ V}$, $p = 5 \text{ Pa}$ and the initial species attributes to be $T_e = 5 \text{ eV}$, $n_{e,0} = 5 \cdot 10^9 \text{ cm}^{-3}$ and $T_i/T_e = 0,008$ respectively.

3.3 Anion Energy Distributions in Oxygen

Chapter 4

Conclusion

Appendix A

Appendix

quantity	equation	relevance
Debye length	$\lambda_{D,j}^2 = \frac{\varepsilon_0 k_B T_j}{n_j e^2}$ $\lambda_D^2 = \left(\lambda_{D,e}^{-2} + \lambda_{D,i}^{-2} \right)^{-1}$	distance around a charge, at which quasi-neutrality is satisfied, λ_D is the combined screening length from individual species
plasma parameter	$N_D = n \frac{4}{3} \pi \lambda_D^3$	number of particles inside Debye sphere, if $N_D \gg 1$ an ionized gas is considered a plasma (degree of ionization)
plasma frequency	$\omega_{p,j}^2 = \frac{n_j e^2}{\varepsilon_0 m_j} = \frac{v_{th,j}}{\lambda_{D,j}} = \frac{1}{\tau_j}$	upper limit for interaction with fields/forces or external excitations inverse screening time
thermal velocity	$v_{th,j}^2 = \frac{k_B T_j}{m_j}$	mean velocity from kinetic theory of gases
coulomb logarithm	$\ln(\Lambda)$ $\Lambda = \frac{b_{\max}}{b_{\min}} = \lambda_D \cdot \frac{4\pi\varepsilon_0\mu v_{th}^2}{e^2}$	dimensionless scale for transport processes inside discharge fraction of probability for a cumulative 90° scattering by many small perturbation collisions and a single right angle scattering
collision frequency	$\nu_j = \frac{e^4 n_j \ln(\Lambda)}{8\sqrt{2m_j}\pi\varepsilon_0(k_B T_j)^{3/2}}$	two body coulomb collision frequency inside species j

quantity	equation	relevance
particle distance & mean free path	$\bar{b} = \frac{\hbar}{m_j v_{th,j}}$ $s_{mfp,j} = \frac{v_{th,j}}{\nu_{j,k}}$	mean inter particle distance for species j free flight between subsequent collisions of species j and k with collision frequency $\nu_{j,k}$
speed of sound	$c_S^2 = \frac{\gamma Z k_B T_e}{m_i}$ $\gamma = 1 + 2/f = 5/3$	speed of longitudinal ion waves at electron pressure adiabatic coefficient with f, the kinetic degree of freedom
Debye-Hückel potential	$\Phi = \frac{Q}{4\pi\epsilon \vec{r} } e^{-\frac{ \vec{r} }{\lambda_D}}$	electrostatic potential of charge particle Q at distance $ \vec{r} $, equal to coulomb interaction with additional shielding by charged particles
drift velocity	$v_{d,j} = u_j = \frac{j_j}{n_j q} = \frac{m\sigma E}{\rho e f}$	average velocity of a particle in a conductor with an electric field applied E , where N is the number of free electrons per atom
electric mobility	$\mu_j = \frac{v_d}{E}$	ability of charged particle of moving through an electric field — with presence of a con- ductor

Table A.1: Selection of physical properties of a low temperature ccrf discharge. The index j denotes the species, e.g. electrons, ions. Used quantities can be found in the preface in table 2.

Bibliography

- [1] F. X. Bronold et al. “Radio-frequency discharges in oxygen: I. Particle-based modelling”. In: *J. Phys. D: Appl. Phys.* 40 (2007), pp. 6583–6592.
- [2] V. A. Godyak, R. B. Piejak, and B. M. Alexandrovich. “An experimental system for symmetric capacitive rf discharge studies”. In: *Rev. Sci. Instrum.* (1990), pp. 2401–2406.
- [3] C. G. Goedde, Allan J. Lichtenberg, and Michael A. Lieberman. “Self-Consistent Stochastic Electron Heating in Radio Frequency Discharges”. In: UCB/ERL M88/29 (1988).
- [4] G. Gozadinos et al. “Collisionless electron heating by capacitive radio-frequency plasma sheaths”. In: *Plasma Sources Sci. Technol.* 10.2 (2001).
- [5] E. Kawamura J. T. Gudmundsson and M. A. Lieberman. “A benchmark study of a capacitively coupled oxygen discharge of the oopd1 particle-in-cell Monte Carlo code”. In: *Plasma Sources Science and Technology* 22.3 (2013), p. 035011.
- [6] D. E. Horne K. Köhler J. W. Coburn and E. Kay. In: *J. Appl. Phys.* 57, 59 (1985).
- [7] H. Kawano and F. M. Page. “Experimental methods and techniques for negative-ion production by surface ionization. Part I. Fundamental aspects of surface ionization”. In: *International Journal of Mass Spectrometry and Ion Physics* 50.1 (1983), pp. 1–33. ISSN: 0020-7381.
- [8] C. Kullig., J. Meichsner, and K. Dittmann. “Detachment-induced electron production in the early afterglow of pulsed cc-rf oxygen plasmas”. In: *Physics of Plasmas* 19 (2012), pp. 73–100.
- [9] M. A. Lieberman. “Analytical solution for capacitive RF sheath”. In: *IEEE Transactions on Plasma Science* 16.6 (1988), pp. 638–644. ISSN: 0093-3813. DOI: 10.1109/27.16552.
- [10] J. Los and J.J.C. Geerlings. “Charge exchange in atom-surface collisions”. In: *Physic Reports* 190.3 (1990), pp. 133–190.
- [11] P. Matthias. *2D Simulation of RF Discharges*. Ernst-Moritz-Arndt Universität Greifswald, Institute of Physics, 2015.
- [12] A. Piel. “Plasma Physics - An Introduction to Laboratory, Space and Fusion Plasmas”. In: (2010), pp. 170 ff., 338 ff.
- [13] S. Scheuer. “Plasmadiagnostische Untersuchungen zur Charakterisierung von Moden in elektronegativen RF-Plasmen”. In: *Master thesis* (2015).
- [14] F. J. Schulze. *Electron heating in capacitively coupled radio frequency discharges*. Ruhr-University Bochum, Fakultät of Physics und Astronomy, 2009.
- [15] M. Surendra and M. Dalvie. “Moment analysis of rf parallel-plate-discharge simulations using the particle-in-cell with Monte Carlo collisions technique”. In: *Phys. Rev. E* 48 (5 1993), pp. 3914–3924. DOI: 10.1103/PhysRevE.48.3914.
- [16] D. Tskhakaya et al. “The Particle-In-Cell Method”. In: *Contrib. Plasma Phys.* 47.8-9 (2007), pp. 563–594.

- [17] D. Tskhakaya et al. “The Particle-In-Cell Method”. In: *Contrib. Plasma Phys.* 47.8-9 (2007), pp. 563–594.
- [18] S. Ustaze et al. “Electron Capture and Loss processes in the Interaction of Hydrogen, Oxygen and Fluorine Atoms and Negative Ions with a MgO(100) Surface”. In: *Physical Review Letters* 79.18 (1997), pp. 3526–3529.

Acknowledgements

The acknowledgments and the people to thank go here, don't forget to include your project advisor...